Journal of The Electrochemical Society, **160** (10) A1847-A1855 (2013)
0013-4651/2013/160(10)/A1847/9/$31.00 © The Electrochemical Society

Analysis of Air Cathode Perfomance for Lithium-Air Batteries

Yun Wang[*,z] **and Sung Chan Cho**

Renewable Energy Resources Lab (RERL), Department of Mechanical and Aerospace Engineering, The University of California, Irvine, California 92697-3975, USA

Lithium-air (Li-air) batteries have a theoretical specific energy comparable to gasolines. The air cathode plays a critical role in battery operation, where oxygen reacts with Li ions and electrons; and discharge products are stored in the pore structure. In major non-aqueous electrolytes, discharge products are insoluble and extremely low in electric conductivity, causing electrode passiviation and raising transport polarization. As discharging proceeds, insoluble materials are deposited at the reaction site and accumulate, increasing voltage loss and eventually shutting down operation. In this work, we present analysis of air cathode performance, taking into account both electrode passivation and transport resistance raised by insoluble products. Both effects are theoretically evaluated and compared. Validation is carried out against experimental data under low currents. The effects of electrode pore structure, such as porosity and tortuosity, on both the influence of insoluble precipitates and discharge capability are investigated.
 [DOI: 10.1149/2.092310jes]

Manuscript submitted June 4, 2013; revised manuscript received July 22, 2013. Published August 29, 2013.

Low energy capability as opposed to fossil fuels remains as a major hurdle to battery development. Metal-oxygen batteries are attractive due to the absence of active cathode material, i.e. oxygen, in energy storage devices. Metal materials such as Fe, Zn, Al, Mg, Ca, Li, etc. have been researched for metal-oxygen batteries.[1] Among them, Li-air batteries show a promising potential of high specific energy storage due to use of lithium metal which is light in weight.[2,3] Bruce et al.[4] reported theoretical values of 3505 Wh kg^{-1} and 3582 Wh kg^{-1} for non-aqueous and aqueous electrolytes, respectively. These values are comparable to those of direct methanol fuel cells (DMFC) (5524 Wh kg^{-1}) and gasoline engine (11,860 Wh kg^{-1}).[5] Its capacity at current stage of Li-air battery development, however, is still much less than the theoretical values.[6] Several major factors are responsible for the limited actual capacity, such as electrolyte consumption and precipitation of lithium oxides inside electrode's pore structure. Figure 1 shows the schematic of a Li-air battery. During discharging, lithium is oxidized in the anode to produce lithium ions and electrons. Electrons flow through external circuit to produce electric work, while lithium ions transport across electrolyte to react with oxygen and electrons in the cathode. During charging, lithium metal is plated out in the anode, and O2 is released in the cathode.

In air cathodes, the pore networks provide paths for both Li ions and oxygen in electrolyte, while the carbon structure conducts electrons. At catalyst surface, oxygen is reduced to produce Li composites, e.g. lithium oxides:

$$Li^+ + e^- + O_2 + * \rightarrow LiO_2^* \quad [1]$$

$$Li^+ + e^- + LiO_2^* \rightarrow Li_2O_2^* \quad [2]$$

where "*" denotes a surface site on Li_2O_2 in which the growth proceeds. Discharge products are usually insoluble in non-aqueous electrolytes, thus their presence may cause pore-network clogging. Because Li oxide composites are in general low in electric conductivity, their coverage over the reaction surface limits electron access to reaction sites, causing electrode passivation. In Li-air batteries, air cathode contributes a major voltage loss, because of the sluggish reaction kinetics and oxygen transport. As discharging proceeds, insoluble discharge products build up in the pore networks and on the reaction surface, increasing both oxygen and electron transport resistances (see Figure 2) and consequent voltage loss.

The first non-aqueous Li-air batteries that exhibit rechargibility were reported[7] by Abraham and Jiang in 1996. Since then, it has been an active area of research to improve the technology through exploring electrochemical reaction mechanisms, structure optimization, and selection of electrolyte and catalysts materials.[8–14] Tran et al.[15,16] added long-chain hydrophobic molecules to activated carbon surface to delay formation of Lithium oxide layer. Yanming et al. reported a specific capacity of 4000 mAh/g_{carbon} by growing Co_3O_4 catalyst on the nickel current collector foam.[17] Xia et al. investigated partially-wetted cathode condition to improve oxygen diffusion in Li-air battery and reported a 60% enhancement of discharge capacity compared to fully flooded cathode.[18] Mirzaeian and Hall studied the impacts of porosity, pore structure, morphology of carbon and surface area of carbon in the air cathode on the specific capacity.[19,20] Yang et al. tested mesocellular carbon foam as the cathode.[21] Through nanocasting technique, the carbon sample of bimodal mesopores with narrow pore size distribution was fabricated, and a Li-air battery using this carbon sample showed about 40% increase in capacity compared to commercial carbon black. Several researchers proposed use of non-carbonate solvents with limited Li_2O_2 solubility or boron-based anion receptor additives to enhance the solubility of Li_2O_2.[22,23] Mitchell et al. reported hollow carbon fibers with 30 nm diameters grown on a ceramic porous substrate for use in the cathode electrode.[24] They reported a high specific capacity with low carbon loading. Lithium oxides grew as nodules on the fibers and developed into toroids during discharge.[25] Andrei et al. and J. Xiao et al.[26] discussed several approaches for improving battery's energy density and optimizing air-cathodes. Zhang et al.[27] employed galvanostatic discharge, polarization, and ac-impedance techniques to study Li-air battery, and showed that the discharge performance of Li/O_2 cells is determined mainly by the carbon air electrode, instead by the Li anode.[28] reported results from a reversible internal redox couple[29] and a first principles metal-insulator-metal charge transport model to probe the electrical conductivity through Li_2O_2 films. Both experiment and theory show a "sudden death" in charge transport when film thickness is ~5 to

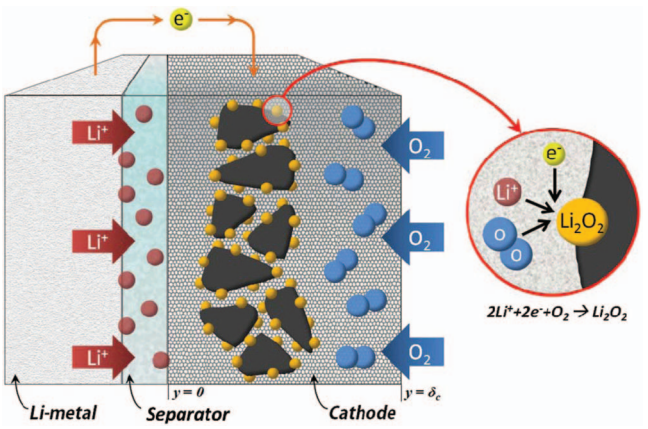

Figure 1. Schematic of a Li-air battery and its discharge operation with discharge product Li_2O_2 as example.

*Electrochemical Society Active Member.
zE-mail: yunw@uci.edu

10 nm. They also indicated that electron tunneling[30,31] may provide the mechanism for electron transport through the films.

In addition to experiment, Albertus et al. proposed a physics-based model accounting for discharge products.[32] Sandhu et al.[33] developed a diffusion-limited model for a Li-air battery using organic electrolyte, and presented transient concentration profiles of the dissolved oxygen in the electrolyte. Nanda et al.[34] reported a three-dimensional spatial distribution of lithium products using neutron tomographic imaging. Higher concentration of lithium oxides was observed near the edge of electrode; and a relatively uniform distribution was observed in the center area. Wang[35] and Hou et al.[36] stressed out that lithium oxides precipitation is similar to water freezing in PEM fuel cells under sub-freezing condition. Wang[35] explained the similarity between ice formation within PEM fuel cells[37,38] and insoluble discharge products in Li-air batteries. They also extended the coverage approach developed in PEM fuel cells to model the effects of insoluble discharge products in batteries, and validated against the data obtained for planar electrodes. In this paper, we follow the knowledge of PEM fuel cells,[39] and develop a similar approach to evaluate voltage loss by electrode passivation due to insoluble products precipitation as opposed to that by oxygen transport resistance. Different with our previous work,[35] the analysis in this paper accounts for oxygen transport resistance, which can be significant in porous electrodes. Porous electrodes exhibit much larger reaction surface area than planar ones, thus they are frequently used in practical battery systems. Further, previous works mostly focus on experiment and numerical simulation (e.g. Ref. 32); whereas fundamental work of theoretical analysis is equally important, for example, analysis that defines dimensionless parameters and compares different mechanisms not only add new knowledge and understanding to the field, but also provide guideline in electrode design and testing. This paper contributes this aspect of Li-air battery development. The oxygen profile in air cathodes is analytically obtained. Comparison with literature experimental data is presented. The analysis consists of two parts: the first one presents theoretical evaluation on spatial variation of several important quantities, such as phase potential and temperature. The second describes the effects of two major mechanisms that insoluble products impact on voltage loss and compares them.

Theoretical Evaluation

In operation, electric energy conversion is not 100% in efficiency. Battery voltage is usually around 2.5–3.0 V, lower than the theoretical voltage. Beside electric energy, the rest is released in form of waste heat. Temperature has profound effects on Li-air battery operation as it determines the capability of overcoming the activation barrier for a reaction. The principle mechanisms for waste heat generation include the reversible and irreversible heating of the electrochemical reactions, and ohmic heating. The reversible and irreversible sources are released at the reaction interface during energy conversion, whereas the ohmic heating arises from the resistance to electric current flows and ion movement. These sources lead to spatially varying temperature inside a battery. To evaluate the upper bound of temperature variation, one can assume all the heating sources were uniformly distributed inside the cathode electrode, the temperature variation can be evaluated by:[39]

$$\Delta T = \frac{I(E' - V_{cell})\delta}{2k^{eff}} \quad [3]$$

where E' is defined as $-\frac{\Delta\bar{h}}{2F}$ and represents the EMF (electromotive force) that all the energy from the Li-oxygen reaction, the 'calorific value', heating value, or enthalpy of formation, were transformed into electrical energy. The effective thermal conductivity k^{eff} is determined by electrode composition and structure. The thermal conductivity of a liquid, if experimentally unavailable, can be evaluated through the theoretical formula by Bridgman in 1923. Later, Power et al.[40] modified the equation, which has been used for pure substances:

$$k_l = 2.8\left(\frac{N}{V}\right)^{2/3}\sigma V_B \quad [4]$$

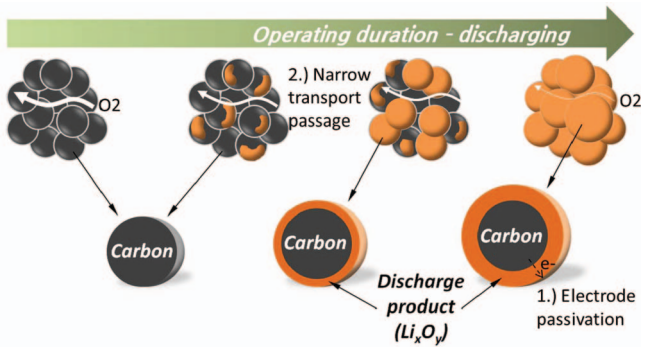

Figure 2. Schematic of the effects of insoluble discharge products on battery performance: 1.) electrode passivation; 2.) raised transport resistance.

where N is the Avogadro's number, V represents the molar volume, σ is the Boltzmann's constant, and V_B denotes the speed of sound. For mixture electrolyte, the Filippov rule can apply to obtain the mixture thermal conductivity k_{1m}:

$$k_{1m} = W_1 k_{11} + W_2 k_{12} - 0.72\,(k_{11} - k_{12})\,W_1 W_2 \quad [5]$$

where k_{11} and k_{12} represents the thermal conductivities for pure component 1 and pure component 2, respectively. W_i is the mass fraction for component i. The components are so chosen that $k_{11} > k_{12}$. This equation has been reported in the open literature to be accurate (within ±5%).[41] The cathode of Li-air batteries is essentially a porous medium containing solid matrix and electrolyte in the pore network. Its effective thermal conductivity k^{eff} is determined by electrode composition and structure, evaluated by:

$$k^{eff} = \sum_{i=1}^{n} \varepsilon_i^{\tau_i} k_i \quad [6]$$

where ε_i and τ_i are the volume fraction and tortuosity of a constituent material i in the cathode electrode, respectively. Among the electrode constituent materials, carbon and metal support such as the Ni mesh are good thermal conductors, and the electrode effective thermal conductivity can be approximated by considering those materials only. To obtain a general sense of temperature variation, k^{eff} of 1.0 W/m K, 2.5 V, and 1 mA/cm^2 will yield around 0.01°C variation, which is negligible. However, a higher current of 0.1 A/cm^2 will lead to a change ~1°C, which causes local reaction variation. Some correlations are listed in Table I.

During discharging, Li^+, oxygen, and electrons are consumed. The primary driving forces for their transport are the gradients of their concentrations (for Li^+ and oxygen) and electric phase potentials (for ions and electrons). Assuming diffusion and migration are the dominant forces for Li^+ transport, and diffusion is the major driven force for oxygen transport, their spatial variations, in absence of bulk flow in electrolyte, can be evaluated through:

$$\frac{\Delta C_e}{C_{e,0}} = \frac{(1-t_+^0)I}{2F}\frac{\delta}{C_{e,0}D_{Ce}^{eff}} \quad \text{or} \quad \Delta C_e = \frac{(1-t_+^0)I}{2F}\frac{\delta}{D_{Ce}^{eff}} \quad [7]$$

and

$$\frac{\Delta C_{O2}}{C_{O2,1}} = \frac{I}{8F}\frac{\delta}{C_{O2,1}D_{O2}^{eff}} \quad \text{or} \quad \Delta C_{O2} = \frac{I}{8F}\frac{\delta}{D_{O2}^{eff}} \quad [8]$$

where $C_{e,0}$ and $C_{O2,1}$ are the concentrations of Li^+ and oxygen at y = 0 and y = δ (see Figure 1), respectively. t_+^0 is the transference number of Li^+ with respect to the velocity of solvent, representing the fraction of the current carried by species Li^+. Depending on electrolyte composition, it can be a function of the electrolyte concentration. The effective coefficients of material properties can be evaluated through the Bruggeman correlation:

$$D_{Ce}^{eff} = \varepsilon^{\tau} D_{Ce}^0 \quad \text{and} \quad D_{O2}^{eff} = \varepsilon^{\tau} D_{O2}^0 \quad [9]$$

Table I. Correlation of the effective thermal conductivity for porous media.

Author	Model	Remarks	Reference
Taine & Petit	$k_{eff}^{Max} = \sum_i \varepsilon_i k_i$ $\frac{1}{k_{eff}^{Min}} = \sum_i \frac{\varepsilon_i}{k_i}$	The simplest model by connecting in series or in parallel the thermal resistance associated with both phases.	42
Maxwell	$k_{eff}^{MXW} = \frac{k_s\left[(1-\varepsilon)\left(2k_s+k_f\right)+3\varepsilon k_f\right]}{(1-\varepsilon)\left(2k_s+k_f\right)+3\varepsilon k_s}$		43
Sadeghi et al.	$k_{eff} = \frac{d}{R_{tot}A} = \frac{4d}{lwR_{tot}}$	Analytically derived for fuel cell's diffusion layer based on the thermal resistance network model.	44
Hashin & Shtrikman	$k_{eff}^{Max} = k_s + \frac{3\varepsilon k_s\left(k_f-k_s\right)}{3k_s+(1-\varepsilon)\left(k_f-k_s\right)}$ $k_{eff}^{Min} = k_f + \frac{3(1-\varepsilon)k_f\left(k_s-k_f\right)}{3k_f+\varepsilon\left(k_s-k_f\right)}$	Modified from[42] by considering a composite system composed of a large number of coated spheres.	45
Bear & Buchlin	$k_{eff} = -2k_s + \frac{1}{\frac{\varepsilon}{2k_s+k_f}+\frac{1-\varepsilon}{3k_s}}$		46
Grant & West	$k_{eff} = \frac{1}{3}X_s k_s + (1-X_s)k_f$	Adopted a 3-D tube unit to evaluate a two-phase system. X_s is the volumetric fraction of tubular inclusions.	47

τ can be empirically set to 1.5 when the exact pore structure is unknown. The electrolyte phase potential variation can be evaluated in a similar way following Ohm's law:

$$\Delta\Phi^{(e)} = \frac{I\delta}{2\kappa^{eff}} \quad [10]$$

where κ^{eff} is related to the volume fraction of ion-conductive materials or directly through experiment measurement. A value of 1 S/m yields a variation of 0.001 V at 1 mA/cm^2 and δ of 0.1 mm. It is negligibly small as opposed to the battery's operating voltage. However, with high current, e.g. 0.1 A/cm^2, or using low-conductivity electrolyte, the variation can be considerable and the resistance becomes a major factor limiting battery performance. Table II lists the ionic conductivity for a number of electrolytes.

In all the above analytical formula, two factors play an important role in determining the spatial variations, they are the operating current density I and cathode electrode thickness δ. Under the conditions of sufficiently small I and δ, the spatial variations can be negligibly small and the above quantities can be treated uniform. As a result, the reaction is uniform across the electrode. In the discussion and analysis below, we assume uniform reaction across the cathode, which is, as shown above, valid for sufficiently small I and δ.

The actual electrochemical reaction kinetics and path are complex, involving a number of reaction steps and intermediates. In the cathode, the oxygen reduction reaction (ORR) occurs. For the ORR at the glassy carbon surface, the following steps may involve:[62,63] $O_2 \rightarrow O_{2(ads)}$; $O_{2(ads)} + e^- \rightarrow [O_{2(ads)}]^-$; $[O_{2(ads)}]^- \rightarrow O_{2(ads)}{}^-$; $O_{2(ads)}{}^- + H_2O \rightarrow HO_{2(ads)} + OH^-$; $HO_{2(ads)} + e^- \rightarrow HO_2{}^-{}_{(ads)}$; $HO_2{}^-{}_{(ads)} \rightarrow HO_2{}^-$. The subscript "ads" denotes adsorption at the reaction surface. The third step was found to be the rate determining step for pH > 10; otherwise, the second was, as suggested by Taylor and Humffray.[64,65] For the sake of simplification, we assume a one-step reaction and approximate the discharge reaction rate by the Tafel equation:

$$j_c = -ai_c = -ai_{0,c}^{ref} C_{O_2}^{1-\beta} C_e^{1-\beta} \exp\left(-\frac{1-\beta}{RT}F\eta\right) \quad [11]$$

where the factor of the surface-to-volume ratio a characterizes the electrode roughness. The surface overpotential η is determined by local phase potentials and equilibrium potential U_o:

$$\eta = \Phi^{(s)} - \Phi^{(e)} - U_o \quad [12]$$

The above assumes no insoluble discharge products are deposited at the reaction surface. Under the extreme condition of negligible spatial variations of temperature, phase potentials, oxygen concentration, and C_e, the exchange current density j_c can be assumed to be uniformly distributed across the cathode.

Analysis and Discussion

During discharging, insoluble Li oxides are produced and deposited at local reaction sites. It is likely the initial precipitation nucleates heterogeneously at preferred sites, followed by thin film formation over reaction surface. For porous electrodes, the following power law is frequently adopted to describe the effect of insoluble precipitates on electrochemical activity:

$$a = a_0\left(1 - \frac{\varepsilon_{prod}}{\varepsilon}\right)^{\tau_a} \quad [13]$$

where $\frac{\varepsilon_{prod}}{\varepsilon}$ represents the volume fraction of insoluble precipitates in the pore space, and τ_a is the exponent coefficient that measures the degree of insoluble products' effect. ε_{prod} is calculated through the reaction rate:

$$\varepsilon_{prod} = \int_0^t -\frac{j_c M_{prod}}{nF\rho_{prod}}dt = \varepsilon_{prod,0} + \frac{IM_{prod}}{n\delta F\rho_{prod}}t \quad [14]$$

where n is the moles of electrons transferred per mole of the product. In addition, the coverage model presented above is more general, encompassing the film resistor model. For the spherical-film growth mode, the exponent coefficient τ_a is given by:[35]

$$\tau_a = -\frac{I(1-\beta)F}{a_0 RT\ln\left(1-\frac{\varepsilon_{prod}}{\varepsilon}\right)}\left\{A_0\left[\sqrt[1/3]{1+\frac{\varepsilon_{prod}}{\varepsilon_{carbon}}}-1\right]r_{carbon}+R_0\right\} \quad [15]$$

The above shows that the coefficient τ_a is proportional to current density I and is a function of ε_{prod}. In porous electrodes, various growth modes of insoluble products occur. The following correlation was proposed by Ref. 35 and adopted in the present paper to account for the effects of current density and insoluble product volume fraction:

$$\tau_a = \begin{cases} B_1\dfrac{I}{I_0} & s < s_0 \text{ where } s = \dfrac{\varepsilon_{prod}}{\varepsilon} \\ \dfrac{I}{I_0}\left[B_1 + B_2(s-s_0)\right] & \text{otherwise} \end{cases} \quad [16]$$

Table II. Ionic conductivity for various electrolytes.

Electrolyte	Ionic conductivity	Remarks	Reference
PVA (Poly Vinyl Alcohol)	$10^{-8} \sim 10^{-4}$ S/cm	PVA complexed with lithium triflate system	48
PC / γ-BL (propylenecarbonate / γ-butyrolactone)	1.7×10^{-3} S/cm	60P(ECH-EO):15PC:10γ-BL:15$LiClO_4$ @ 363K	49
DMF / γ-BL dimethylformamide / γ-butyrolactone)	2.8×10^{-3} S/cm	60P(ECH-EO):15DMF:10γ-BL:15$LiClO_4$ @ 363K	
PVA(15)–PMMA(10)–LiBF4(8)– EC(67)	9.0377×10^{-3} S/cm		
PVA(15)–PMMA(10)–LiBF4(8)– PC(67)	2.4855×10^{-3} S/cm	@373K	50
PVA(15)–PMMA(10)–LiBF4(8)– DEC(67)	0.2022×10^{-3} S/cm		
PVA(15)–PMMA(10)–LiBF4(8)– GBL(67)	1.1523×10^{-3} S/cm		
PVdF- HFP	2×10^{-3} S/cm		51
PVC / PMMA	1.4×10^{-3} S/cm	@ room temperature	52
PAN(21)–PEO(2)– $LiCF_3SO_3$ (8)–PC(27.7)–EC(41.3)	1.713×10^{-3} S/cm		
PAN(21)–PEO(5)– $LiCF_3SO_3$ (8)–PC(24.7)–EC(41.3)	8.492×10^{-3} S/cm	@373K	53
PAN(21)–PEO(10)– $LiCF_3SO_3$ (8)–PC(27.7)–EC(33.3)	80.950×10^{-3} S/cm		
PAN(21)–PEO(15)– $LiCF_3SO_3$ (8)–PC(24.7)–EC(31.3)	23.880×10^{-3} S/cm		
EC(38) –PC(33) –PAN(21) –$LiClO_4$(8)	3.5×10^{-3} S/cm		
EC(42) –PC(36) –PAN(15) –$LiCF_3SO_3$(7)	2.2×10^{-3} S/cm		
EC(62) –PC(13) –PAN(16) –PEGDA(1) –$LiClO_4$(8)	3.0×10^{-3} S/cm	@323K	54
EC(68) –PC(15) –PEGDA(3) –$LiClO_4$(14)	8.0×10^{-3} S/cm		
EC(35) –PC(31) –PVP(24) – $LiCF_3SO_3$ (10)	1.0×10^{-3} S/cm		
EC–$LiClO_4$	$10^{-8} \sim 10^{-7}$S/cm	[EC]/[$LiClO_4$] = 0.5 @ 298K	
	10^{-6}S/cm	[EC]/[$LiClO_4$] = 1.0 @ 298K	55
	$10^{-5} \sim 10^{-4}$ S/cm	[EC]/[$LiClO_4$] = 2.0 @ 298K	
PEO(22.7) –PAN(17.4) –PrC(7.3) –EC(8.5) –$LiClO_4$(4.3)	0.37×10^{-3} S/cm	HSPE @ 303K	56
PEO(22.7) –PrC(13.3) –$LiClO_4$(1.2)	0.84×10^{-3} S/cm	PEO + PrC @ 303K	
PAN(23.2) –PrC(24.5) –EC(28.4) –$LiClO_4$(3.0)	1.34×10^{-3} S/cm	PAN + PrC + EC @ 303K	
PC-DME	10^{-3} S/cm	(1:1 by wt) plasticized P($LiOEG_nB$) n = 3, 5, 9	57
	12×10^{-3} S/cm	(1:1 by vol.) 1M $LiClO_4$ @ 293K	
	14×10^{-3} S/cm	(1:1 by vol.) 1M $LiPF_6$ @ 293K	
EC-DMC	8×10^{-3} S/cm	(1:1 by vol.) 1M $LiClO_4$ @ 293K	58
	10×10^{-3} S/cm	(1:1 by vol.) 1M $LiPF_6$ @ 293K	
	11.7×10^{-3} S/cm	(1:1 by mol) 1M $LiPF_6$ @ 303K	59
	$< 10^{-3}$ S/cm	(1:2 by wt) plasticized P($LiOEG_nB$) n = 3	60
	5.52×10^{-3} S/cm	1mol LiF + 1mol $(C_6F_5)_3B$ in DME	
DME	7.43×10^{-3} S/cm	1mol CF_3CO_2Li + 1mol $(C_6F_5)_3B$ in DME	61
	5.52×10^{-3} S/cm	1mol $C_2F_5CO_2Li$ + 1mol $(C_6F_5)_3B$ in DME	

Another effect of insoluble discharge products is to raise oxygen transport resistance: as oxygen dissolved in the electrolyte is transported via the pore network, presence of insoluble precipitates narrows down the passage, reducing oxygen diffusivity. Assuming the film is firmly packed without any pore structure, the effective diffusivity can be modified following the Bruggeman correlation:

$$D_{O2}^{eff} = \varepsilon^{\tau_d} D_{O2}^0 = \left(\varepsilon_0 - \varepsilon_{prod}\right)^{\tau_d} D_{O2}^0 \qquad [17]$$

The exponent coefficient τ_d represents the tortuosity of diffusion path. The 1-D transport equation in porous electrodes can be written as follow:

$$\frac{\partial \varepsilon C_{O2}}{\partial t} + \frac{\partial u C_{O2}}{\partial x} = \frac{\partial}{\partial x}\left(D_{O2}^{eff} \frac{\partial C_{O2}}{\partial x}\right) + \frac{j_c}{4F} \qquad [18]$$

In common operation, no external forces are imposed to promote electrolyte bulk flow. The mass consumption by the electrochemical reactions, however, can induce mass flow. In PEM fuel cells, the electrochemical reaction gives rise to gaseous mass flow of around ~0.1 m/s during operation. Provided that the common electrochemical reaction rate in Li-air batteries is much weaker than that in PEM fuel cells, and the battery electrolyte is either liquid or solid, the induced mass flow, if it is liquid, is negligibly small in Li-air batteries, thus convection can be neglected. The time constant of oxygen diffusion across an electrode is estimated by:

$$\tau_{diff} = \frac{\delta^2}{D_{O2}^{eff}} \qquad [19]$$

For an electrode of δ~100 μm, τ_{diff} is around 10 s and 100 s for D_{O2}^{eff} of 10^{-9} m^2/s and 10^{-10} m^2/s, respectively. Both are small relative to the discharging duration of Li-air batteries. Thus, we neglect the transient term in the analysis.

Furthermore, the consumption rate of oxygen is determined by the electrochemical reaction rate which in turn depends on local oxygen content. Analytically solving the coupled oxygen transport and electrochemical reaction is challenging, particularly when accounting for the effects of insoluble products on oxygen diffusivity and consumption. One way to evaluate the associated voltage loss is to follow the approach in PEM fuel cells:[39] we assume the cathode consists of a number of independent reactors operated under constant current; through evaluating overpotential spatial variation, we will be able to assess the voltage loss associated with oxygen transport. As the reaction is uniform, the local reaction rate is then expressed by $j_c = -\frac{I}{\delta}$; and the oxygen concentration can be analytically obtained by solving Eq. 18:

$$C_{O2}(y) = C_{O2,\delta} - \frac{I}{8F} \frac{\delta^2 - y^2}{\delta D_{O2} \left(\varepsilon_0 - \varepsilon_{prod}\right)^{\tau_d}} = C_{O2,\delta}\left[1 - Da \frac{1 - \left(\frac{y}{\delta}\right)^2}{\varepsilon_0^{\tau_d - \tau_{d,0}} \left(1 - \frac{\varepsilon_{prod}}{\varepsilon_0}\right)^{\tau_d}}\right] \qquad [20]$$

where the dimensionless parameter Da is called the Damköhler number, defined by:

$$Da = \frac{I}{8F} \frac{\delta}{C_{O2,\delta} D_{O2} \varepsilon_0^{\tau_{d,0}}} = \frac{\text{Reaction rate}}{\text{Mass transport rate}} \qquad [21]$$

A current density of 0.1 mA/cm^2 or 1 A/m^2, δ of 0.1 mm, ε_0 of 0.75, $\tau_{d,0}$ of 1.5, and D_{O2} of 10^{-9} m^2/s yield Da~0.04 for $C_{O2,\delta}$ of

5 mol/m^3 (5 mM), clearly indicative of sufficiently fast mass diffusion relative to the reaction kinetics under the discharging current density. *Da* is larger under higher tortuosity, e.g. *Da*~0.053 for $\tau_{d,0}$ of 2.5, respectively. It is of interest to evaluate the oxygen concentration drop across the electrode:

$$\Delta C_{O2} = C_{O2,\delta} - C_{O2,0} = Da \frac{C_{O2,\delta}}{\varepsilon_0^{\tau_d - \tau_{d,0}} \left(1 - \frac{\varepsilon_{prod}}{\varepsilon_0}\right)^{\tau_d}} \quad \text{or}$$

$$\frac{\Delta C_{O2}}{C_{O2,\delta}} = \frac{Da}{\varepsilon_0^{\tau_d - \tau_{d,0}} \left(1 - \frac{\varepsilon_{prod}}{\varepsilon_0}\right)^{\tau_d}} \quad [22]$$

$\frac{\Delta C_{O2}}{C_{O2,\delta}}$ is small (<15%) at 0.1 mA/cm^2, $\tau_{d,0} = \tau_d = 1.5$, ε_0 of 0.75, *Da* of 5 × 10^{-2} and $\frac{\varepsilon_{prod}}{\varepsilon_0}$<0.5. For $\frac{\varepsilon_{prod}}{\varepsilon_0}$~0.8, $\frac{\Delta C_{O2}}{C_{O2,\delta}}$~56% which is significant. The oxygen profile of Eq. 20 is substituted into Eq. 11, yielding the below overpotential:

$$\Delta\eta = \frac{RT}{(1-\beta)F}\left(\tau_a \ln\left(1 - \frac{\varepsilon_{prod}}{\varepsilon_0}\right) + (1-\beta) \times \ln\left(1 - Da \frac{1 - \left(\frac{y}{\delta}\right)^2}{\varepsilon_0^{\tau_d - \tau_{d,0}} \left(1 - \frac{\varepsilon_{prod}}{\varepsilon_0}\right)^{\tau_d}}\right)\right) = \Delta\eta_a + \Delta\eta_{O2} \quad [23]$$

where

$$\Delta\eta_a = \frac{RT\tau_a \ln\left(1 - \frac{\varepsilon_{prod}}{\varepsilon_0}\right)}{(1-\beta)F} \quad \text{and}$$

$$\Delta\eta_{O2} = \frac{RT}{F} \ln\left(1 - Da \frac{1 - \left(\frac{y}{\delta}\right)^2}{\varepsilon_0^{\tau_d - \tau_{d,0}} \left(1 - \frac{\varepsilon_{prod}}{\varepsilon_0}\right)^{\tau_d}}\right)$$

The voltage loss associated with the increased oxygen transport resistance can be assessed through the associated overpotential at a representative site: the middle-depth location of the electrode, i.e.

$$\Delta\eta_{O2}\left(y = \frac{\delta}{2}\right) = \frac{RT}{F} \ln\left(1 - \frac{3Da}{4\varepsilon_0^{\tau_d - \tau_{d,0}} \left(1 - \frac{\varepsilon_{prod}}{\varepsilon_0}\right)^{\tau_d}}\right) \quad [24]$$

This enables direct comparison of the two mechanisms that insoluble precipitates affect the electrochemical reaction, i.e., electrode passivation and increased oxygen transport resistance. A parameter β_3 can be defined as the ratio of these two overpotentials:[39]

$$\beta_3 = \frac{\Delta\eta_a}{\Delta\eta_{O2}\left(y = \frac{\delta}{2}\right)} = \frac{\frac{RT\tau_a \ln\left(1 - \frac{\varepsilon_{prod}}{\varepsilon_0}\right)}{(1-\beta)F}}{\frac{RT}{F} \ln\left(1 - \frac{3Da}{4\varepsilon_0^{\tau_d - \tau_{d,0}} \left(1 - \frac{\varepsilon_{prod}}{\varepsilon_0}\right)^{\tau_d}}\right)} = \frac{\tau_a \ln\left(1 - \frac{\varepsilon_{prod}}{\varepsilon_0}\right)}{(1-\beta) \ln\left(1 - \frac{3Da}{4\varepsilon_0^{\tau_d - \tau_{d,0}} \left(1 - \frac{\varepsilon_{prod}}{\varepsilon_0}\right)^{\tau_d}}\right)} \quad [25]$$

For an idealized case - the spherical-film growth mode of precipitates, substituting Eq. 15 into Eq. 25 and assuming $\tau_d = \tau_{d,0}$ yield:

$$\beta_{3,spherical} = \frac{-IF\left\{A_0\left[\sqrt[1/3]{1 + \frac{\varepsilon_{prod}}{\varepsilon_{carbon}}} - 1\right] r_{carbon} + R_0\right\}}{a_0 RT \ln\left(1 - \frac{3Da}{4\left(1 - \frac{\varepsilon_{prod}}{\varepsilon_0}\right)^{\tau_d}}\right)} = \frac{-IF\left\{A_0\left[\sqrt[1/3]{1 + \frac{\varepsilon_{prod}}{\varepsilon_0}\frac{\varepsilon_0}{1-\varepsilon_0}} - 1\right] r_{carbon} + R_0\right\}}{a_0 RT \ln\left(1 - \frac{3Da}{4\left(1 - \frac{\varepsilon_{prod}}{\varepsilon_0}\right)^{\tau_d}}\right)} \quad [26]$$

$\frac{\varepsilon_0}{1-\varepsilon_0}$ represents the volumetric ratio of the pore space and solid matrix. For small $\frac{\varepsilon_{prod}}{\varepsilon_0}$, $\frac{3Da}{4(1-\frac{\varepsilon_{prod}}{\varepsilon_0})^{\tau_d}}$ is a small value, and $-\ln(1 - \frac{3Da}{4(1-\frac{\varepsilon_{prod}}{\varepsilon_0})^{\tau_d}})$ can be approximated by $\frac{3Da}{4(1-\frac{\varepsilon_{prod}}{\varepsilon_0})^{\tau_d}}$. Thus, it is clear that $\beta_{3,film}$ is large under small $\frac{\varepsilon_{prod}}{\varepsilon_0}$. As example, for $\frac{\varepsilon_{prod}}{\varepsilon_0}$<0.25, $\frac{3Da}{4(1-\frac{\varepsilon_{prod}}{\varepsilon_0})^{\tau_d}}$<0.058 or $-\ln(1 - \frac{3Da}{4(1-\frac{\varepsilon_{prod}}{\varepsilon_0})^{\tau_d}}) < 0.06$, yielding $\beta_{3,film}$>9 for A_0 of 8.5 × 10^7 Ω m^2, a_0 of 100, T of 298 K, ε_0 of 0.75, *I* of 0.1 mA/cm^2, τ_d of 1.5, and r_{carbon} of 40 nm.[35] In another words, the voltage loss due to oxygen transport limitation is much smaller than that of electrode passivation in the range of operation ($\frac{\varepsilon_{prod}}{\varepsilon_0}$<0.25). As $\frac{\varepsilon_{prod}}{\varepsilon_0}$ is over 0.85, $\beta_{3,film}$<0.25, indicative of the dominant effect of oxygen transport limitation.

For crude evaluation, the total voltage loss associated with formation of insoluble products, i.e. the oxygen transport limitation and electric passivation, can be approximated using the following equation:

$$\Delta\eta = \Delta\eta_a + \Delta\eta_{O2}\left(y = \frac{\delta}{2}\right) \quad [27]$$

In below, we will present comparison with several experimental data. A similar set of model parameters were used in the comparison for all the experimental data, listed in Table III. As the preceding analysis was performed under low current density (0.1 mA/cm^2 or lower), in all the experimental data, low current density, either 0.1 mA/cm^2 and 0.05 mA/cm^2, were chosen for comparison. Figure 3 and Figure 4 compare the analytical solutions with experimental data from Read.[68] Acceptable agreements are achieved: the first stage of

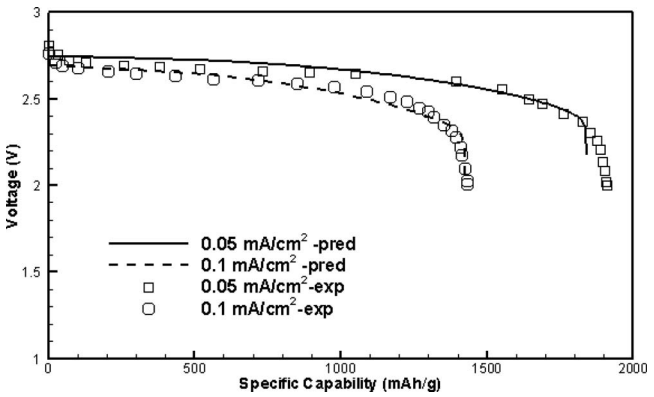

Figure 3. Comparison of the analytical solution with the experimental data from Ref. 68. The experiment was conducted on a Li-air battery using a PVDF air cathode (case 1).

Table III. Physical, electrochemical, and model parameters.

Description	Unit	Value
Temperature	°C	25
Transfer coefficient β		0.5
Faraday constant	C/mol	96,487
Electrical conductivity of cathode electrode	S/m	∼10
O_2 diffusivity in electrolyte	m^2/s	9×10^{-10}
O_2 solubility[66]		0.00876 in DME with of 1 M Li^+
Cathode thermal conductivity[67]	W/m K	∼1.0
Tortuosity τ (case 1,3,4/case 2)		1.8/2.4
Electrode porosity, ε_0		0.75
Electrode thickness, δ	mm	0.1–1
Density of discharge product (Li_2O_2/ Li_2CO_3)	kg/ m^3	2140/2110
Molecular weight of discharge product (Li_2O_2/Li_2CO_3)	kg/mol	0.04588/0.07389
A_0	Ω m^2	8.5×10^7
I_0	A m^{-2}	0.6
B_1 in Eq. 16 [35]		2.5
B_2 in Eq. 16 (case 1,2,4 [35]/case 3)		8/12
s_0 in Eq. 16 (case 1,2,3/case 4 [35])		0.2/0.4

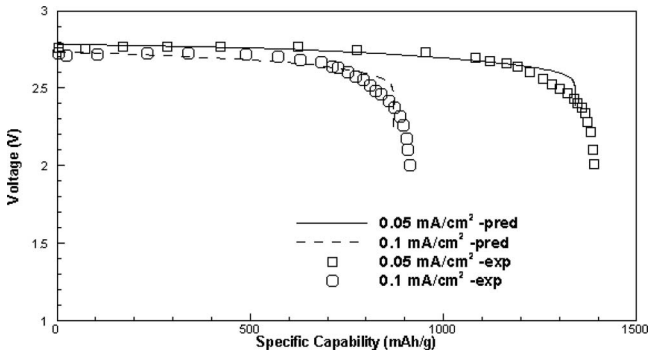

Figure 4. Comparison of the analytical solution with the experimental data from Ref. 68. The experiment was conducted on a Li-air battery using a PTFE air cathode (case 2).

gradual decrease arises from electrode passivation due to precipitation of insoluble discharge products at the reaction surface; the latter fast drop is caused by the raised oxygen transport resistance due to insoluble materials occupying pore space. Discrepancy appears at the rapid drop stage of voltage: the predictions of the analytical solution show rapid decrease, whereas the drops of the experimental data are relatively slow. In the analytical approximation, we use the middle-length site as the reference to approximate the polarization associated with the raised oxygen transport resistance, which may cause the discrepancy.

Figure 5 and Figure 6 compare model predictions with experimental data from the work of Zhang et al.[69] and Wang et al.[70] Again, acceptable agreements were achieved for both cases. The electrolytes used in the experiments are similar to that of Read[68] in the previous comparison, as shown in Table IV. As 2.0 V is usually set as the cut

Table IV. List of electrolytes for experimental cases.

Case #	Electrolyte	Reference
Case 1	1 M LiPF6 PC:DME	68
Case 2	1 M LiPF6 PC:DME	68
Case 3	1 M LiTFSI in PC–DME (1:1 by wt)	69
Case 4	1 M LiTFSI in PC/EC (1:1 ratio by wt) with 50 wt% DME	70

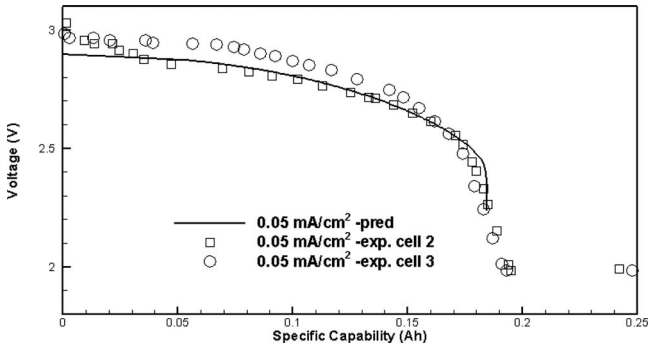

Figure 5. Comparison of the analytical solution with the experimental data from Ref. 69. The experiment was conducted on a Li-air battery using an air cathode (EC/KB/PTFE) and 1.0 M LiTFSI in PC-DME (1:1 by weight) as the electrolyte (case 3).

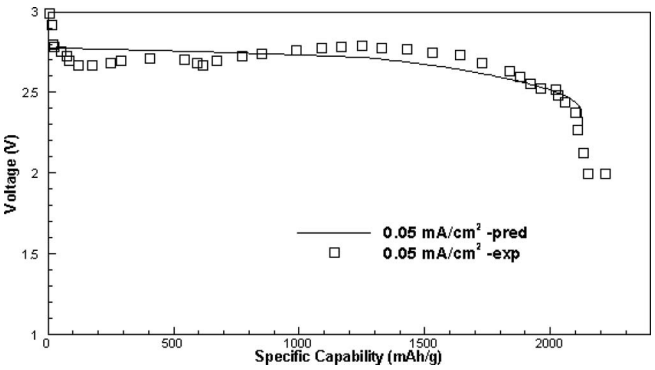

Figure 6. Comparison of the analytical solution with the experimental data from Ref. 70. The experiment was conducted on a Li-air battery using an air cathode (KB/PTFE 85:15 by wt) and 1 M LiTFSI in PC/EC (1:1 ratio by wt) with 50 wt% DME as the electrolyte (case 4).

voltage, voltage drop reduces the duration of discharge operation, and the battery's energy capability. As explained before, the Da number measures the importance of mass transport in a reaction system; and the pore-network characteristics, porosity and tortuosity, are the major factors determining the value of Da: small porosity provides few passages for oxygen diffusion, reducing oxygen accessibility to the reaction site; torturous passages lengthen the diffusion path, reducing the effective oxygen diffusivity. Both factors affect discharge voltage loss and thus the energy capability of Li-air batteries. Figures 7 and 8 display the discharge voltages under varying porosity and tortuosity, respectively, showing the battery performance differs significantly. As porosity is reduced from 0.9 to 0.5, the specific capacity decreases by

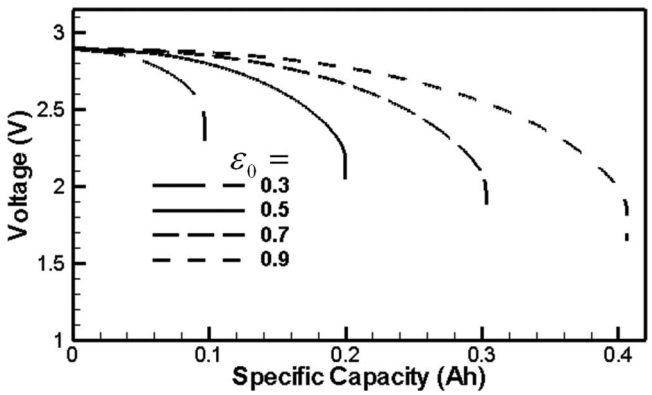

Figure 7. Li-air battery performance under varying electrode porosity.

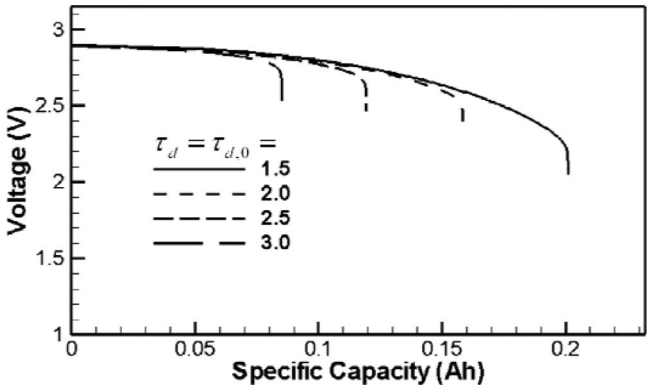

Figure 8. Li-air battery performance under varying electrode tortuosity.

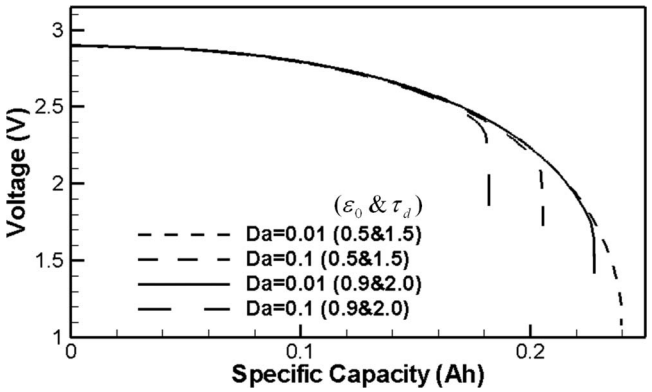

Figure 10. Li-air battery performance under varying Da numbers.

almost half. When tortuosity increases from 1.5 to 3.0, the capacity is reduced by more than half. In the analytical results, other electrode properties used are the same as Figure 5 or Case 3.

In addition, both factors influence the effects of insoluble discharge products. Figure 9 displays the discharge voltages under different values of the two factors but with the same Da number. Note that the defined Da number characterizes the importance of diffusion relative to reaction at the initial stage without insoluble precipitates, and lumps porosity and tortuosity as well as other factors. Though the Da number is same for all the cases, the discharge voltages differ due to the impacts of tortuosity and porosity on the insoluble precipitates' effects.

Figure 10 presents the batter performance when varying the value of the Da number. It is seen that under lower Da the battery exhibits a larger capacity, as expected. The Da number, defined in this paper, evaluates relative importance of the reaction rate over the diffusion rate at the initial stage of discharging or in absence of discharging insoluble products. A small Da number shows the species diffusion is relative fast, relative to the species' reaction rate. Thus, a smaller Da number in electrode design yields a higher battery capacity. Note that the Da number lumps several parameters including tortuosity, initial porosity, current density, and electrode thickness. Under the same Da number, the battery capacity can be further optimized through tortuosity and initial porosity, as also indicated by Fig. 9.

The electrode structural characteristics play an important role in battery performance. Though in fabrication the Da number can be designed to be small (e.g. <0.1), thus oxygen transport is not a limiting factor. However, insoluble discharge products precipitate in the pore structure, reducing effective diffusivity and further discharging capability. To improve the electrochemical kinetics, micro-/meso-scale pores are usually used, which exhibit high specific area (surface area per volume) for the reaction. Small pores, however, lead to reduced

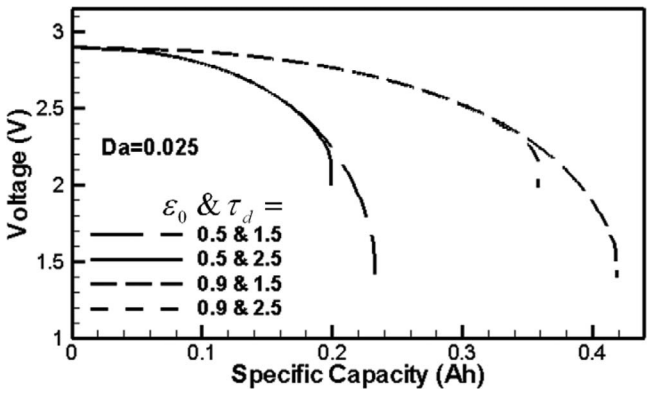

Figure 9. Li-air battery performance under varying electrode properties. The Da numbers are set the same for all the four curves.

effective diffusivity due to either high tortuosity or shift in diffusion mechanism. In addition, gas can be trapped within pores by electrolyte during fabrication process, particularly in small hydrophobic pores. Two types of diffusion processes are frequently encountered in gas phase in micro-systems: they are molecular diffusion and Knudsen diffusion. The latter occurs in situations in which gas molecules collide more frequently with pore walls than with other gas molecules. This type of diffusion is encountered when the mean free path of gas molecules is of the order of the pore characteristic length scale (when the Kn number is much larger than 1). The mean free path of oxygen molecules ($\lambda_{molecule} = \frac{8RT}{\sqrt{2}\pi D^2 NaP}$) is ca 0.1 μm. Thus, in micro-/meso-scale pores (the pore size < 0.1 μm), the Knudsen diffusion is important. The Knudsen diffusion coefficient in a long straight pore can be calculated through the kinetic theory of gases:

$$D_K^{O2} = \frac{2r_{pore}}{3}\sqrt{\frac{8RT}{\pi M^{O2}}} \quad [28]$$

The value of D_K^{O2} is around $2.64 \times 10^{-5} m^2/s$ when r_{pore} = 0.1 μm, which is much higher than that in liquid/solid electrolyte. Oxygen diffusivity in liquid electrolytes can be evaluated using a hydrodynamic model, which assumes that the resistance of solute molecule movement is caused by the viscous force, similar to a particle movement in a viscous fluid. In a dilute liquid, the approach results in the famous Stokes–Einstein equation: $D^{O2} = \frac{k_B T}{6\pi r \mu}$, where k_B is the Boltzmann's constant, r the radius of the oxygen molecule, and μ the electrolyte viscosity. This equation yields oxygen diffusivity in the range of $10^{-8} - 10^{-11}$ m^2/s.[71,72] Furthermore, in liquid electrolyte the Knudsen diffusion is in general unimportant because of the small molecular free path (around the scale of the molecular dimension). Thus, electrolyte with gas trapped in pore structure can significantly improve oxygen transport, therefore improving discharge capability. However, presence of gas pores reduces the reaction surface area by cutting Li+ access. Thus, for optimization purpose the pore structure and electrolyte composition in electrodes need to be carefully designed.

Conclusions

In this work, we presented a modeling and analysis study on the effects of insoluble products on cathode performance in discharging operation of Li-air batteries. The spatial variations of important quantities including temperature, species concentrations, and phase potentials were analyzed and evaluated. Under low discharge current density (e.g. <0.1 mA/cm^2) or thin cathode thickness, spatial variations of these quantities are small and can be neglected. The oxygen profile across the battery cathode was analytically obtained, and the concentration variation was related to the Da number. The Da number is ~0.05 @ 0.1 mA/cm^2, and thus diffusion resistance is insignificant when insoluble precipitates are absent. We further evaluated the voltage loss due to the increased oxygen transport resistance arising from

presence of insoluble discharge precipitates. To compare the effects of raised oxygen resistance and electric passivation, a dimensionless parameter was defined as the ratio of the overpotentials caused by these two mechanisms. Through evaluating this parameter, we found that the effect of electric passivation is dominant when the volume fraction of insoluble discharge product is low (<50%), i.e. at the initial stage of discharge; while the raised oxygen transport resistance is significant when the volume fraction of insoluble discharge products is high. An approximation model was formulated to evaluate the overall voltage loss due to insoluble discharge products precipitation, and showed acceptable agreement with experimental data in the literature under low currents. The pore-network structure of electrodes, including porosity and tortuosity, plays an important role in discharge capability. High tortuosity and low porosity not only reduce the value of Da, but also affect the effects of insoluble precipitates on voltage loss. The developed analytical formula can be directly applied for electrode design to optimize pore structure (porosity and tortuosity) and electrolyte composition.

List of Symbols

a	factor of effective catalyst area per unit volume when discharge product is present
a_o	factor of catalyst surface area factor per unit volume
C	molar concentration, mol/m^3
D	species diffusivity, m^2/s
F	Faraday's constant, 96,487 C/equivalent
I	current density, A/cm^2
i	superficial current density, A/cm^2
j	transfer current density, A/cm^3
M	molecular weight, kg/mol
R	universal gas constant, 8.134 J/mol K; Ohmic resistance, mΩ cm^2
t	time, s
T	temperature, K

Greek

β	transfer coefficient
ρ	density, kg/m^3
ϕ	phase potential, V
κ	ionic conductivity, S/m
ε	porosity or volume fraction
η	surface overpotential, V
τ	tortuosity/coverage coefficient
δ	thickness, m

Superscripts and Subscripts

abs	absorption
c	cathode
d	diffusion
e	electrolyte
eff	effective value
o	reference value; initial value

References

1. K. Kinoshita, *Metal/Air Batteries. In Electrochemical Oxygen Technology*, K. Kinoshita, Ed.; John Wiley & Sons, Inc.: New York (1992).
2. G. Girishkumar, B. McCloskey, A. C. Luntz, S. Swanson, and W. Wilcke, *J. Phys. Chem. Lett.*, **1**, 2193 (2010).
3. J. Christensen, P. Albertus, R. S. Sanchez-Carrera, T. Lohmann, B. Kozinsky, R. Liedtke, J. Ahmed, and A. Kojic, *J. Electrochem. Soc.*, **159**(2), R1 (2012).
4. P. G. Bruce, S. A. Frauberger, L. J. Hardwick, and J.-M. Tarascon, *Nat. Mater.*, **11**, 19 (2012).
5. DOE Properties of Fuels (2006).
6. S. S. Zhang, D. Foster, and J. Read, *J. Power Sources*, **195**(4), 1235 (2010).
7. K. M. Abraham and Z. Jiang, *J. Electrochem. Soc.*, **143**, 1 (1996).
8. Y. Gao, C. Wang, W. Pu, Z. Liu, C. Deng, P. Zhang, and Z. Mao, *Int. J. of Hydrogen Energy*, **37**(17), 12725 (2012).
9. C. O. Laoire, S. Mukerjee, and K. M. Abraham, *J. Phys. Chem. C*, **113**, 20127 (2009).
10. Y. Li, J. Wang, X. Li, D. Geng, R. Li, and X. Sun, *Chem. Comm.*, **47**, 9438 (2011).
11. A. Debart, J. Bao, G. Armstrong, and P. G. Bruce, *J. Power Sources*, **174**, 1177 (2007).
12. Y. Lu, Z. Xu, H. A. Gasteiger, S. Chen, K. Hamad-Schifferli, and Y. Shao-Horn, *J. Am. Chem. Soc.*, **132**, 12170 (2010).
13. Y. Lu, H. A. Gasteiger, M. C. Parent, V. Chiloyan, and Y. Shao-Horn, *Electrochem. Solid-State Lett.*, **13**, A69 (2010).
14. Y. C. Lu, D. G. Kwabi, K. P. C. Yao, J. R. Harding, J. Zhou, L. Zuin, and Y. Shao-Horn, *Energy & Environmental Science*, **4**, 2999 (2011).
15. C. Tran, J. Kafle, X. Q. Yang, and D. Qu, *Carbon*, **49**, 1266 (2011).
16. C. Tran, X. Q. Yang, and D. Qu, *J. Power Sources*, **195**, 2057 (2010).
17. Y. Cui, Z. Wen, and Y. Liu, *Energy Environ Sci.*, **4**, 4727 (2011).
18. C. Xia, C. L. Bender, B. Bergner, K. Peppler, and J. Janek, *Electrochem. Comm.*, **26**, 93 (2013).
19. M. Mirzaeian and P. Hall, *J. Power Sources*, **195**(19), 6817 (2010).
20. M. Mirzaeian and P. J. Hall, *Electrochim. Acta*, **54**, 7444 (2009).
21. X. Yang, P. He, and Y. Xia, *Electrochem. Comm.*, **11**(6), 1127 (2009).
22. S. J. Visco, E. Nimon, and L. C. De Jonghe, *Encyclopedia of Electrochemical Power Sources*, Elsevier, Amsterdam, 376 (2009).
23. B. Xie, H. S. Lee, H. Li, X. Q. Yang, J. McBreen, and L. Q. Chen, *Electrochem. Comm.*, **10**, 1195 (2008).
24. R. R. Mitchell, B. M. Gallant, C. V. Thompson, and S. H. Yang, *Energy Environ. Sci.*, **4**, 2952 (2011).
25. P. Andrei, J. P. Zheng, M. Hedrickson, and E. J. Pichta, *J. Electrochem. Soc.*, **157**(12), A1287 (2010).
26. J. Xiao, D. Wang, W. Xu, R. E. Williford, J. Liu, and J. Zhang, *J. Electrochem. Soc.*, **157**(4), A487 (2010).
27. S. S. Zhang, D. Foster, and J. Read, *J. Power Sources*, **195**, 1235 (2010).
28. V. Viswanathan, K. S. Thygesen, J. S. Hummelshøj, J. K. Nørskov, G. Girishkumar, B. D. McCloskey, and A. C. Luntz, *J. Chem. Phys.*, **135**, 214704 (2011).
29. R. R. Gagne, C. A. Koval, and G. C. Lisensky, *Inorg. Chem.*, **19**(9), 2854 (1980).
30. M. Uiberacker, Th. Uphues, M. Schultze, A. J. Verhoef, V. Yakovlev, M. F. Kling, J. Rauschenberger, N. M. Kabachnik, H. Schröder, M. Lezius, K. L. Kompa, H.-G. Muller, M. J. J. Vrakking, S. Hendel, U. Kleineberg, U. Heinzmann, M. Drescher, and F. Krausz, *Nature*, **446**, 627 (2007).
31. M. Razavy, *Quantum Theory of Tunneling*, World Scientific Publishing Co. (2003).
32. P. Albertus, G. Girishkumar, B. McCloskey, R. S. Sanchez-Carrera, B. Kozinsky, J. Christensen, and A. C. Luntz, *J. Electrochem. Soc.*, **158**, A343 (2011).
33. S. Sandhu, J. Fellner, and G. Brutchen, *J. Power Sources*, **164**, 365 (2007).
34. J. Nanda, H. Bilheux, S. Voisin, G. M. Veith, R. Archibald, L. Walker, S. Allu, N. J. Dudney, and S. Pannala, *J. Phys. Chem. C*, **116**(15), 8401 (2012).
35. Y. Wang, *Electrochimica Acta*, **75**, 239 (2012).
36. J. Hou, M. Yang, M. W. Ellis, R. B. Moore, and B. Yi, *Phys. Chem. Chem. Phys.*, **14**, 13487 (2012).
37. J. Mishler, Y. Wang, P. P. Mukherjee, R. Mukundan, and R. L. Borup, *Electrochimica Acta*, **65**, 127 (2012).
38. Y. Wang, P. P. Mukherjee, J. Mishler, R. Mukundan, and R. L. Borup, *Electrochimica Acta*, **55**, 2636 (2010).
39. Y. Wang, *J. Electrochem. Soc.*, **154**, B1041 (2007).
40. R. B. Bird, W. E. Stewart, and E. N. Lightfoot, *Transpon Phenomena*, John Wiley & Sons, Inc., Aug. (1978).
41. D. S. Jung and D. A. Didion, EPRI Report, ER-6364, Research Project 8006-2, May (1989).
42. J. Taine and J.-P. Petit, Transferts thermiques—Mécanique des fluids anisothermes, Dunod Université (1989).
43. J. C. Maxwell, *A Treatise on Electricity and Magnetism*, Clarendon Press (1892).
44. E. Sadeghi, M. Bahrami, and N. Djilali, *J. Power Sources*, **179**(1), 200 (2008).
45. Z. Hashin and S. A. Shtrikman, *J. Appl. Phys.*, **33**, 3125 (1962).
46. J. Bear and J. M. Buchlin, *Modeling and Application of Transport Phenomena in Porous Media*, Kluwer Academic Publishers, Boston (1991).
47. F. S. Grant and G. F. West, *Interpretation Theory in Applied Geophysics*, McGraw-Hill Book Company, New York (1965).
48. H. A. Every, F. Zhou, M. Forsyth, and D. R. MacFarlane, *Electrochimica Acta*, **43**, 1465 (1998).
49. N. Nithya, S. Selvasekarapandian, P. C. Selvin, D. A. Kumar, and J. Kawamura, *Electrochimica Acta*, **66**(1), 110 (2012).
50. S. Rajendran, M. Sivakumar, and R. Subadevi, *Materials Letters*, **58**, 641 (2004).
51. K. M. Abraham and S. B. Brummer, in: J. P. Gabano (Ed.), Lithium Batteries, Academic Press, New York, 371 (1983).
52. H. J. Rhoo, H. T. Kim, J. K. Park, and T. S. Hwang, *Electrochimica Acta*, **42**(10), 1571 (1997).
53. S. Rajendran, T. Mahalingam, and R. Kannan, *Solid State Ionics*, **130**, 143 (2000).
54. K. M. Abraham and M. Alamgir, *J. Electrochem. Soc.*, **137**(5), 1657 (1990).
55. M. Watanabe, M. Kanba, K. Nagaoka, and I. Shinohara, *Journal of Polymer Science: Polymer Physics Edition* **2**, 939 (1983).
56. N. Munichandraiah, G. Sivasankar, L. G. Scanlon, and R. A. Marsh, *J. Appl. Polym. Sci.*, **65**(11), 2191 (1998).
57. W. Xu and C. A. Angell, *Electrochimica Acta*, **48**, 2029 (2003).
58. W. V. Schalkwijk and B. Scrosati, *Advances in Lithium-Ion Batteries*, Springer (2002).
59. P. Birke, S. Doring, S. Scharner, and W. Weppner, *Ionics*, **2**, 329 (1996).
60. W. Xu and C. A. Angell, *Electrochimica Acta*, **48**, 2029 (2003).
61. X. Sun, X. Q. Yang, H. S. Lee, and J. McBreen, *Proc. of the 194th Electrochemical Society Meeting*, BNL-66142, CONF-981108, Boston (1998).
62. E. Yeager, *J. Mol. Catal.*, **38**, 5 (1986).
63. J. Zhang, *PEM Fuel Cell Electrocatalysts and Catalyst Layers: Fundamentals and Applications*, Springer, (2008).

64. R. J. Taylor and A. A. Humffray, *J. Electroanal. Chem.*, **64**, 63 (1975).
65. R. J. Taylor and A. A. Humffray, *J. Electroanal. Chem.*, **64**, 85 (1975).
66. J. Read, K. Mutolo, M. Ervin, W. Behl, J. Wolfenstine, A. Driedger, and D. Foster, *J. Electrochem. Soc.*, **150**, A1351 (2003).
67. Y. Wang, K. S. Chen, J. Mishler, S. C. Cho, and X. C. Adroher, *Applied Energy*, **88**, 981 (2011).
68. J. Read, *J. Electrochem Soc.*, **149**, A1190 (2002).
69. J.-G. Zhang, D. Wang, W. Xu, J. Xiao, and R. E. Williford, *J. Power Sources*, **195**, 4332 (2010).
70. D. Wang, J. Xiao, W. Xu, and J.-G. Zhang, *J. Electrochem. Soc.*, **157**(7), A760 (2010).
71. G. K. Batchelor, *J. Fluid Mech.*, **74**, 1 (1976).
72. W. M. Deen, *Analysis of Transport Phenomena*, Oxford University Press (1998).